Enhancement of depletion forces by electrostatic depletant repulsion

4 **AUTHORS**, INCLUDING:

Stefano Buzzaccaro
Politecnico di Milano
20 PUBLICATIONS **237** CITATIONS

SEE PROFILE

Roberto Piazza
Politecnico di Milano
118 PUBLICATIONS **3,114** CITATIONS

SEE PROFILE

Jader Colombo
ETH Zurich
10 PUBLICATIONS **76** CITATIONS

SEE PROFILE

Enhancement of depletion forces by electrostatic depletant repulsion

Stefano Buzzaccaro,[1] Roberto Piazza,[1,a)] Jader Colombo,[2] and Alberto Parola[2]
[1]*Dipartimento CMIC, Politecnico di Milano, via Ponzio 34/3, 20133 Milano, Italy*
[2]*Dipartimento di Fisica e Matematica, Università dell'Insubria, Via Valleggio 11, 22100 Como, Italy*

A large variety of engaging phenomena stems from the occurrence of short-ranged attractive depletion forces. Yet, so far, most experimental studies have been interpreted on the basis of the simple Asakura–Oosawa model, where the depletion agent can be regarded as ideal. Here, conversely, we focus on a system where strong electrostatic coupling is present in the suspension. Specifically, from measurements of equilibrium sedimentation profiles, we obtain an equation of states for a colloidal system where depletion forces are tuned by the addition of a surfactant. At fixed colloid volume fraction, colloidal aggregation takes place when the surfactant concentration reaches a critical value which *rises* for increasing ionic strength. Screening repulsive electrostatic interactions inhibits the depletion mechanism and weakens the effective colloid-colloid attraction. The metastable coexistence curve displays the universal scaling behavior predicted for short-ranged potentials. The experimental data are compared with the theoretical predictions of a simple model which includes only electrostatic interactions. The effective depletion force on the colloids is evaluated by using the hypernetted-chain equation of liquid state theory at different salt concentrations. This model provides a convincing interpretation of the observed enhancement of the depletion mechanism by Coulomb repulsion. © *2010 American Institute of Physics.*
[doi:10.1063/1.3366690]

I. INTRODUCTION

The investigation of the systems of colloidal particles interacting via attractive depletion forces has yielded valuable and often unforeseen insights on the contingency of the liquid state and on the origin of metastable gel and glassy phases.[1–3] In particular, two recent studies[4,5] have unraveled the close relation between the occurrence of a metastable liquid-liquid gap within the phase diagram of short-ranged depletion systems and gelation, which can be consistently depicted as an arrested spinodal decomposition process. Short-ranged interactions due to depletion effects are commonly induced by adding either nonadsorbing polymers or surfactants, which self-aggregate in the form or globular micelles, to a colloidal suspension. So far, most theoretical and experimental studies have focused on a simple approximation, known as the Asakura–Oosawa (AO) model,[6,7] where the depletant D behaves as an ideal gas interacting with the colloidal particles P via a hard-sphere potential. A large amount of experimental evidence[8,9] shows that the AO model does indeed predict some distinctive features of the phase diagram of colloidal suspensions and, for very small D/P size ratio, turns into the very simple "adhesive hard-sphere" (AHS) limit[10] widely used to describe many complex fluid phenomena including protein crystallization.[11]

Yet, the AO model is often just a crude approximation to the variety of physical phenomena taking place in an experimental system: interparticle interactions of different physical origins often modify and enrich the simple AO picture. For instance, an ingenious emulsion fractionation method developed by Bibette *et al.*[12] at the dawning of depletion studies exploited as depletant a charged micellar solution, which cannot be for sure regarded as ideal. Theoretical studies give some general hints to nonideality corrections, showing, in particular, that depletant self-interactions yield two diametrically opposed effects.[13] A repulsively interacting surfactant leads to an increase in the osmotic pressure, leading, according to the standard excluded volume picture, to an *increase* in depletion forces. However, at the same time the depletant gets more and more correlated and structured, something that should rather *reduce* depletion attraction. For binary additive hard-sphere mixtures, this latter effect is predicted to be dominant[14] but, so far, experimental indications are mostly qualitative.

The aim of this work to highlight and quantitatively account for additional depletion attraction that is actually *brought in* by repulsive Coulomb interactions between the components. In particular, the equation of states (EOS) of spherical colloids in the presence of ionic surfactant witnessed that electrostatic coupling substantially strengthens the depletion attraction even if the colloidal particles, which are themselves charged, become more repulsive. By reducing the ionic strength, rapid particle segregation effects, marking the onset of the metastable liquid-liquid separation in the colloidal phase diagram, take place at a lower surfactant concentration. The low-density branch of the metastable coexistence curve, both in the absence of added salt and in the high screening limit, is found to obey the scaling predictions for very short-ranged potentials. Conversely, for sufficiently strong attraction, the dense phase is found to lie within the coexistence gap and displays the behavior of a disordered solid stemming from the kinetic arrest of the settling particle

a)Electronic mail: roberto.piazza@polimi.it.

clusters. Liquid state theories allow a quantitative interpretation of the observed phenomena, showing that they result from the competition of two contrasting effects: while the colloid-micelle repulsion favors a smooth monotonic attractive potential, the micelle-micelle repulsion triggers a significant accumulation of micelles near the surface of the colloids, which may lead to repulsive shoulders in the effective interaction. For a suitable choice of the parameters, the balance between the two trends can indeed promote the aggregation of the colloids through an enhanced depletion mechanism.

This paper is organized as follows. We first present the experimental systems and methods, providing also an overview of the main findings. Then, we develop a simple theoretical model embodying the key physical features of the real system and we discuss the choice of parameters able to describe this colloid-micelle suspension. Finally, EOSs and transition lines at different ionic strengths are compared to the experimental results.

II. EXPERIMENTAL SYSTEMS

A. Colloidal system

The colloids we have used are aqueous suspensions of Hyflon™ MFA, a copolymer of tetrafluoroethylene and perfluoromethylvinylether (PF-MVE) produced by Solvay-Solexis (Bollate, Italy). While pure polytetrafluoroethylene is almost a fully crystalline polymer, usually formed by emulsion polymerization of polydisperse rod-shaped particles, the addition of PF-MVE, bestowing a larger flexibility to the chains, yields monodisperse spherical particles, which can be envisioned as a polycrystalline assembly embedded into an amorphous matrix.[15] For the particle we have used to investigate charged depletant effects, dynamic light scattering yields an average radius of 90 nm and a polydispersity of about 4%. The preliminary measurements discussed in Sec. III have instead been performed with the same MFA batch used in Ref. 4 made of slightly smaller MFA particles ($R \simeq 82$ nm), but with similar figures for what concerns polydispersity and surface charge density. The surface of MFA latex particles bears a negative charge, mostly due to the presence of trapped fluorinated surfactant used in the emulsion polymerization[15] and possibly to added ionic stabilizers. Although no detailed proprietary information is released by the producing company, this is directly witnessed, for the specific sample we used, by the high intrinsic stability of the original dispersion in the presence of a substantial amount of added salt. In all what follows, therefore, we shall assume that the bare MFA particle charge is high enough to fully satisfy the requirements for charge renormalization (see the following discussion).

The approach we have followed fully exploits the unique material and optical properties of MFA polymer colloids, which have been extensively investigated in the past.[15] Here, we only recall that MFA has a very low average refractive index $n \simeq 1.352$, which allows measuring concentrate suspensions with negligible multiple scattering effects. Low optical contrast is a property shared by other colloids, such as PMMA in decalin/tetralin mixtures, but a really distinctive property of MFA particle is that, being partially crystalline, they are also optically anisotropic so that their scattering is partially depolarized. For simplicity, we shall model MFA particles as uniaxial birefringent scatterers, characterized by principal refractive indices $n_\parallel$ and $n_\perp$, and therefore by an average refractive index $n_p = (n_\parallel + 2n_\perp)/3$ and an optical anisotropy $\Delta n = n_\parallel - n_\perp$. Provided that the single crystallites within a particle are small compared to the wavelength, and assuming an incident polarization perpendicular to the scattering plane, the horizontal (I_{VH}) and vertical (I_{VV}) polarization components of the intensity scattered by N interacting particles at wave vector q read, apart from unimportant multiplicative constants, as[15]

$$I_{VH} = N(\Delta n)^2,$$

$$I_{VV}(q) = N[(n_p - n_s)^2 P(q)S(q)] + cI_{VH}, \tag{1}$$

where n_s is the refractive index of the solvent, $P(q)$ and $S(q)$ are, respectively, the form and structure factors, and c is a constant related to fluctuations in the degree of crystallinity, ideally equal to 4/3 for optically monodisperse particles. The main feature of Eq. (1) is that, at variance with I_{VV}, the depolarized intensity I_{VH} depends neither on the optical contrast $n_p - n_s$ nor on the interparticle interactions, being actually q-independent. It can therefore be regarded as an optical analogs of incoherent neutron scattering, which is proportional solely to the number of particles N in the scattering volume and can be then profitably exploited as a probe of the local particle concentration.

Finally, the very high material density of MFA $\rho = 2.14$ g/cm³, combined with its lack of swelling in most inorganic and organic solvent, allows for a precise determination of the particle volume fraction Φ in the suspensions, which we have evaluated from measurements of the suspension density using a high-resolution Paar oscillating-capillary densitometer. As a further bonus, the high value of $\Delta\rho = \rho - \rho_s$, where ρ_s is the solvent density, yields a non-negligible Stokes settling velocity $v_S \simeq 0.02$ μm/s, making equilibrium sedimentation experiments much less time consuming than for other common colloidal lattices.

B. Depletion agent

Most of the experiments have been performed using sodium dodecyl sulfate (SDS) as a depletion agent. The physical properties of aqueous solutions of SDS, a simple anionic surfactant with molecular weight of $M_{SDS} = 288$ Da, have been extensively investigated in the past.[16] Beyond a critical micellar concentration (cmc) that depends on the ionic strength I (decreasing from 8.3 mM in pure water to 0.9 mM for $I = 200$ mM), SDS forms globular micelles with a pretty constant hydrodynamic radius of $a \simeq 2.5$ nm. Their aggregation number N, and therefore structural charge Z, is around 80–110, varying by no more than $\pm 10\%$ up to an ionic strength of $I \simeq 0.4M$. Beyond this value, the micellar morphology becomes elongated and N consistently grows.

For comparison, we shall also present some measurement performed on MFA suspensions in the presence of Triton X100, a widely used nonionic surfactant, with molecular

weight of $M_w = 625$ Da, formerly used in the experiment presented in Ref. 4. As for most nonionic surfactant, Triton cmc (approximately 0.2 mM) is much lower than for SDS. Beyond the cmc, Triton forms in water slightly oblate ellipsoidal micelles with major and minor semiaxes equal to a $= 4.75$ nm and b $= 2.35$ nm, and an aggregation number N $= 145$.[17] Hydration of the ethylene oxide groups constituting Triton hydrophilic heads yields about 20 water molecules per surfactant molecules, which are part of the micelle volume. Triton micelles are characterized by an excluded volume interactions plus an attractive tail. However, at room temperature the reduced second osmotic virial coefficient is rather small, $B_2 \simeq 0.2$, suggesting that the two contributions almost balance, making Triton, to a fair approximation, an ideal uncharged depletion agent.

C. Sedimentation measurements

Measurements of the equilibrium sedimentation profiles consist of detecting the depolarized scattered intensity I_{VH} as a function of the distance z from the sample bottom by vertically translating the cell and using the intensity scattered by the original homogeneous suspension for calibration [in what follows, this method will therefore be dubbed as scanning depolarized light scattering (SDLS)]. The experimental apparatus basically consists of a custom-made light scattering setup, operating at a fixed scattering angle of 90°. Selection of the incident and detected polarization of the scattered intensity is made by means of two Glan–Thomson polarizers (Bernhard Halle, Berlin) with an extinction ratio better than 10^{-6}. The sample cell is mounted on a dc-motorized micrometric translator, allowing cell positioning with a resolution of 0.1 μm and an absolute accuracy and bidirectional repeatability of about 3 μm. An incident He–Ne laser beam is mildly focused in the cell to a spot size of $w_0 \simeq 50$ μm, corresponding to a Rayleigh range, which fixes the maximum useful optical path in the cell, of about 10 mm. A telescope system, embodied in the photodetection systems, allows imaging the sample and limiting the scattering volume using the horizontal and vertical slits. The whole setup is enclosed into a removable hood, allowing one to control the temperature to better than 0.5 °C. Cell translation and data acquisition are controlled by a 16 bit A/D interface board using custom-made software. Sedimentation profiles are acquired using a typical scan speed of 10–20 μm/s.

I_{VH} measurements allow one to obtain accurate sedimentation profiles with a spatial resolution of less than 50 μm in a volume fraction range covering almost four decades. A numerical integration of the particle volume fraction profile $\Phi(z)$ directly yields the local osmotic pressure

$$\Pi(z) = \Delta \rho g \int_z^h \Phi(z) dz, \qquad (2)$$

where h is the height of the cell, and therefore, by pairing the corresponding values for $\Phi(z)$ and $\Pi(z)$, the full EOSs $\Pi(\Phi)$.

An alternative method, which does *not* require optically anisotropic particles (but still particles which can be almost index matched with the solvent), consists of detecting as a function of z the deflection that a laser beam suffers by passing through the inhomogeneous refractive index profile associated with the concentration gradients built up by sedimentation, which is done by monitoring the position of the transmitted beam via a position-sensitive detector.[18] This measurement actually yields the *derivative* of the concentration profile so that discontinuous jumps corresponding to the phase equilibria cannot be properly quantified. For continuous profiles, however, the additional numerical integration required to obtain the EOS yield smoother results than depolarized scattering measurements. Moreover, absolute calibration can still be performed by requiring that the integral of the profile, which is related to the total number of particle in the sample, remains constant. Finally, this beam-deflection method has also the crucial advantage of being reliable even for quite turbid samples since multiple scattering minimally influences the results, providing then a useful cross-check of the results obtained by depolarized scattering.

III. CHARGED PARTICLES WITH ALMOST-IDEAL DEPLETANT

Before considering depletion forces between MFA particles induced by a charged surfactant, let us briefly consider, for a useful comparison, the behavior of MFA suspensions in the presence of Triton X100. This preliminary study is basically an extension of the measurements we already performed at high ionic strength[4] to a condition where the electrostatic coupling between the colloidal particles is tuned by adding salt. We shall then first recall some qualitative observation made in this latter study.

In our system, Triton plays both the role of steric stabilizer for the particles and of depleting agent. When added to MFA dispersions, the surfactant first adsorbs on the particle surface, forming a monolayer that stabilizes the suspension up to very high ionic strength. The full adsorption isotherm can be directly obtained by static light scattering, which shows that full surface coverage is obtained for a surfactant concentration of $c_{s0} \simeq 0.06c$, where c is the particle concentration in g/cm^3, yielding a thickness of the adsorbed layer of about 3 nm. For such a value of the surfactant concentration, the volume fraction of free Triton in solution, as checked by UV spectrophotometry, does not exceed 2 $\times 10^{-3}$. Triton in excess of c_{s0} solubilize only in micelles, acting as depletion agents. The micellar volume fraction can be simply evaluated as[19]

$$\Phi_s = \frac{V_m \mathcal{N}_A}{N M_w}(c_s - c_{s0}) \simeq 1.4(c_s - c_{s0}),$$

where c_s is the concentration of Triton in g/cm^3, $V_m = 4\pi a^2 b/3$ is the volume of a micelle, and $\mathcal{N}_A$ is the Avogadro number.

Depending on Φ_s, the samples display two radically different kinds of behavior. While for $\Phi_s \lesssim 0.105$ they remain transparent and sediment very slow, samples with higher surfactant concentration show a sudden increase in turbidity, witnessing strong fluctuations of concentration, followed by rapid settling at a speed almost three orders of magnitude larger than the typical Stokes settling velocity v_S, leading in
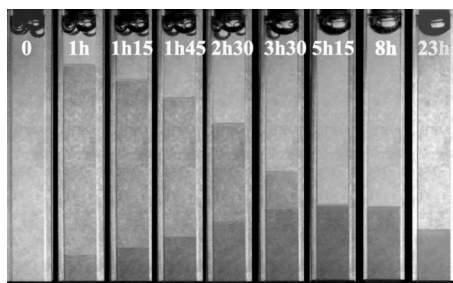
FIG. 1. Fast sedimentation kinetics of a MFA suspension in the presence of a sufficient amount of Triton X100.

a few hour to the formation of a dense sediment. The latter restructures then very slowly, but still remains much more expanded than the sediments eventually obtained at low Φ_s. The transition between these two different regimes is abrupt and reversible: an increase of less than $\Delta\Phi_s=0.07$ in micellar volume fraction leads a transparent sample to become turbid and sediment fast. Nonetheless, if the surfactant content in the supernatant is slightly diluted by the addition of a few drops of water, the fully restructured sediment obtained after weeks rapidly dissolves by gentle agitation, yielding a stable suspension. A typical settling kinetics for a sample display-ing fast sedimentation is shown in Fig. 1.

The equilibrium sedimentation profiles of a number of suspensions left settling for about 6 months allowed one to obtain the EOSs as a function of Φ_s. A key feature of the latter is that, whereas slowly settling samples always display equilibrium between a fluid and an ordered crystal phase, rapid sedimentation almost always yields a single phase, whose featured closely match what is predicted for disor-dered gels or attractive glasses. The Noro–Frenkel general-ized law of the corresponding states,[20] stating that all short-ranged spherically symmetric attractive potentials are characterized by the same thermodynamics properties if compared at the same reduced density and virial coefficient, was then used to map the experimental phase boundaries onto the phase diagram predicted for short-ranged depletion potential with the very small range set by the micelle/particle size ratio.

The most noticeable feature of the results presented in Ref. 4 is that *all* rapidly settling samples are placed within, or very close to, the metastable liquid-liquid (L-L) separation gap in the theoretical phase diagram,[21] suggesting to regard gelation as an arrested phase-separation process. In other words, the spinodal decomposition process taking place by crossing the L-L phase boundary speeds up so much the phase-separation process that the suspension gets trapped into a frozen disordered state, whereas this never takes place for slowly settling samples, although they *do* cross, during the settling process, the theoretical attractive glass line in the phase diagram. Moreover, since the L-L coexistence curve of short-ranged potentials is very flat, the binodal and spinodal lines are actually so close that phase separation occurs at roughly the same value of Φ_s provided that the initial particle volume fraction is not very low. Fast sedimentation can be therefore regarded as a basic clue for locating the L-L phase-
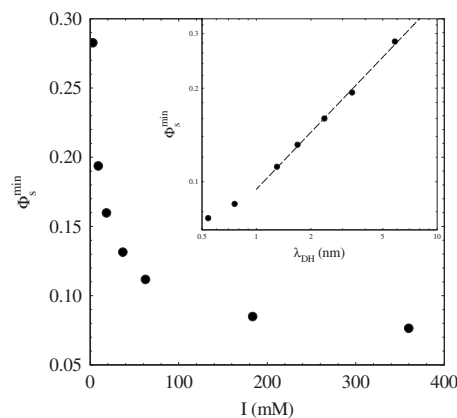

FIG. 2. Ionic strength dependence of the minimum amount of Triton X100 required to phase separate a MFA suspension at particle volume fraction $\Phi=0.01$. The same data are plotted as a function of the Debye–Hückel screening length in the double-log inset, with a power law fit (dashed line).

separation boundary, a crucial observation that will be a guiding line for the present paper.

All the aforementioned experiments were performed in the presence of about $0.1M$ NaCl,[22] corresponding to an electrostatic screening length that is shorter than the range of the attractive depletion potential. An increase in electrostatic coupling, leading to the presence of a competing longer range Coulomb repulsion, can be first of all expected to weaken depletion. Let us then consider the dependence of the minimal micellar volume fraction Φ_s^{min} required to in-duce rapid phase separation versus the solution ionic strength, varied by the addition of NaCl. Samples were pre-pared at several different values of the salt concentration, at fixed particle volume fraction Φ, and for a micellar concen-tration Φ_s variable in steps of $\Delta\Phi_s=0.04$. The value of Φ_s^{min} was fixed by visually checking for rapid sedimentation ef-fects, which indicates those samples lying within the un-stable region. Figure 2, which refers to experiments per-formed at $\Phi=0.01$, shows indeed that Φ_s^{min} rapidly grows by reducing the salt concentration, while it starts to level off to a value of $\Phi_s^{min}\simeq0.07$ only for ionic strength values exceed-ing a few hundreds of millimolar. The inset shows that, as a function of the screening length, Φ_s^{min} actually grows ap-proximately as a power law, with a fitting exponent of about 0.6. We point out that, were Triton micelles considered as spheres with an equivalent hydrodynamic radius of $r=(3V_m/4\pi)^{1/3}\simeq4.2$ nm, the high ionic strength limit for Φ_s^{min} would be about a factor of 2 *lower* than the value Φ_s^{min} predicted for the lower boundary of the metastable L-L curve of the AO model with the same size ratio $q\simeq0.04$.[23] Con-versely, a fair quantitative agreement is found by taking into account that the effective volume swept by the ellipsoidal micelles is larger by a factor of $a/b\simeq2.1$ than the volume of the equivalent sphere.

There are, however, some additional observations that are not directly conveyed in Fig. 2. First of all, for $I<3$ mM, the evidence of phase separation is no longer sharp, but becomes quite fuzzy: instead of gels, fluidlike sediments lacking any apparent yield stress form more slowly (on the time scale of a day) at the cell bottom, without any evidence of a clear meniscus separating the supernatant
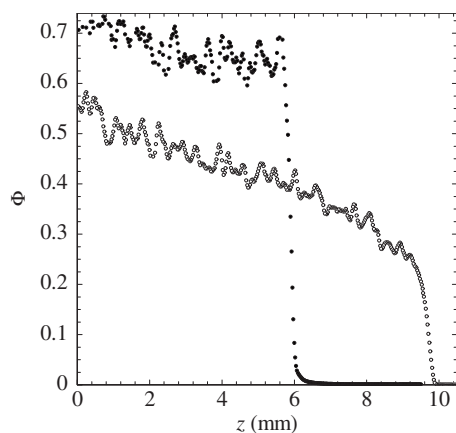
FIG. 3. Sedimentation profiles for MFA suspensions in the presence of 30 mM (full dots) and 60 mM (open dots) NaCl.

from a settling phase. This indicates that colloid segregation takes place through a different mechanisms, possibly through the formation of finite-size cluster that have been predicted[24,25] and experimentally observed[26] for competing potentials. Presently, however, we do not have sufficient evidence to make this claim. In any case, for $I \lesssim 1$ mM, phase separation seems to be completely suppressed, at least up to a surfactant volume fraction of about 30% (beyond which Triton is in a liquid crystalline phase, quite hard to be properly handled). By increasing the initial colloid volume fraction to 10%, the experimental observations become even more intriguing. The onset of fast settling is indeed no longer so sharp and is often preceded by a moderately rapid deposition at the cell bottom of a dense phase, although a sharp meniscus is lacking. This evidence suggests that the phase-separation scenario may be rather different from what was observed in Ref. 4 and possibly that the nature of the separating phase might depend on the strength of the interparticle repulsion.

To investigate this issue, we have followed the sedimentation of five samples prepared at fixed surfactant concentration of $\Phi_s = 0.15$ and initial particle volume fraction of $\Phi \simeq 0.11$, whereas I was varied between 20 and 250 mM. For this value of Φ_s, all samples lie well within the phase-separation region, and therefore sediment fast. Yet, the equilibrium sedimentation profiles obtained by SDLS after 6 weeks, when no further slow rearrangement is detectable, show striking differences. While samples with $I \gtrsim 60$ mM display moderately concentrated sediments with smoothly varying profiles, those profiles obtained at $I \lesssim 30$ mM are much steeper and their sediment much denser. The profiles for samples corresponding to the lower and, respectively, upper limits of these two distinct regions, displayed in Fig. 3, show that particle concentration along the profile obtained at 60 mM varies continuously, growing rather sharply up to $\Phi \simeq 0.25$ and then more slowly up to a value at the cell bottom, which is not much lower than the random close-packing limit for hard spheres. Conversely, the profile obtained for $I = 30$ mM suddenly jumps to a value that is *not* compatible with a disordered phase and, although much flatter (indicating a very small sediment compressibility), reaches at the cell bottom a concentration rather close to the

ordered packing limit. A more detailed analysis shows that an upper fluid phase, although with very low concentration (yielding an ideal barometric profile), is still present over the top of this dense sediment.

As discussed in Ref. 4, these two different profile shapes typify, respectively, dense gels (or attractive glasses) and AHS colloidal crystals. Therefore, although a spinodal decomposition process seems to occur even at rather low ionic strength, the phase-separation scenario seems to be very different, driving the system to crystallization and not to an arrested disordered phase. At variance with what was found in Ref. 4 at low ionic strength, L-L phase separation does not seem to be a sufficient condition for gelation, an observation in agreement with recent numerical simulations.[27] Qualitatively, repulsive interactions may allow for larger particle restructuring, leading to an easier formation of crystalline nuclei, but a full assessment of this suggestion requires further experimental studies. Nonetheless, our measurements quantitatively confirm the intuitive guess that repulsive interparticle interaction considerably hinders depletion.

IV. CHARGED PARTICLES WITH CHARGED DEPLETANT

A. Phase-separation line in the presence of SDS

We discuss now the main topic of this paper, namely, the effective interparticle interactions in MFA suspensions induced by the presence of SDS and the phase behavior they lead to. First, aiming to unravel phase-separation effects in the presence of a charged depletant, we have basically mimicked the measurement performed in the case of Triton. The experiments were performed following the same protocol described in Sec. III and consisted of detecting the lower concentration of SDS micelles needed to induce fast sedimentation in MFA suspensions at $\Phi = 0.02$ as a function of the total ionic strength. Notice that the latter also includes a contribution by nonmicellized SDS. Actually, the cmc in the absence of added salt sets a lower limit of about 8 mM for the minimum ionic strength that can be reached in the experiments, limiting therefore the Debye–Hückel length to a value $\lambda_{DH} \lesssim 3.5$ nm, which is comparable to the size of a SDS micelle, but *much smaller* than the colloid radius. Experiments with SDS differ from those with Triton in another aspect since SDS seems to adsorb very weakly on MFA particle surface. Indeed, at variance with what has been previously found with other perfluorinated particles,[28] the addition of SDS yields practically no increase in the scattered intensity. Negligible surface adsorption is also found by checking, via refractive index measurements, the amount of SDS retained in the supernatant of phase-separated samples (see the following discussion). Such a limited surface adsorption is probably due to the high negative surface charge of the MFA batch we have used, which strongly hinders binding of the anionic surfactant. We shall therefore assume that the surfactant concentration in micellar form c_s (in g/l) is given by the difference between the amount of the surfactant actually added to the solvent and the (ionic strength dependent) cmc.

Our experimental results, presented in Fig. 4, show that, at variance with what has been found for Triton, all samples
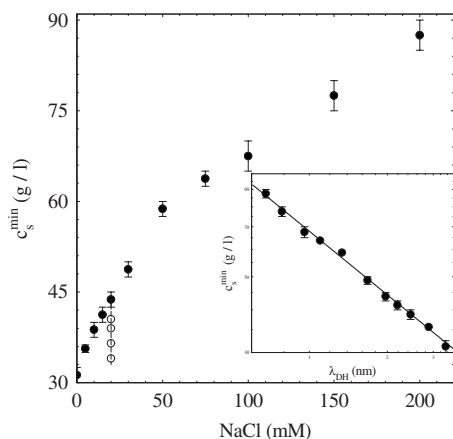
FIG. 4. Phase transition curve of MFA with SDS depletant as a function of added salt (full dots). State points where sedimentation profiles have been measured are shown as open dots. The data are plotted in the double-log inset as a function of λ_{DH} and fitted with a power law $c_s^{min} = a\lambda_{DH}^{-b}$, with $b \simeq 0.6$.

displayed a sharp value for c_s^{min} even at the lowest accessible ionic strength, which, however, decreases by decreasing the salt concentration, witnessing a consistent *increase* in depletion efficiency at low ionic strength. The inset also shows that, at least within this ionic strength range, c_s^{min} displays an approximate power-law trend with the Debye screening length, $c_s^{min} = a\lambda_{DH}^{-b}$, with a phenomenological exponent that is around $b \simeq 0.6$.

B. EOSs

The phase-separation boundary is, however, a rather indirect signature of the effective interactions between MFA colloidal particles; much more detailed information can be obtained by extracting the full EOS via equilibrium sedimentation experiments. To this aim, we have prepared four samples at the initial particle concentration of $\Phi \simeq 0.13$, varying the surfactant concentration at fixed NaCl concentration of 20 mM. The main body of Fig. 4, where the locations of these samples on the phase diagram are displayed as open dots, shows that all of them lie in the stable region. The samples were then left settling and restructuring for about 2 months, and the equilibrium sedimentation profiles were eventually obtained by SDLS measurements. The compressibility factors $Z(\Phi) = \Pi / \rho k_B T$ obtained from the numerical integration of the concentration profiles are shown in Fig. 5, together with a fit of $Z(\Phi)$ with the sticky spheres EOS, derived from the Baxter solution of the Percus–Yevick integral equation by using the compressibility route. Each curve is labeled by the stickiness parameter τ. We see that this simple model is able to reproduce moderately well the experimental EOSs within the uncertainties of the data. The agreement is, however, less satisfactory than what has been obtained in Ref. 4 in high salt conditions, probably indicating that the thermodynamic behavior stemming from the richer features of the interparticle interaction potential is only partly captured by the simplified AHS model (see the following discussion). The fitted values for τ should then be considered just as indicative.
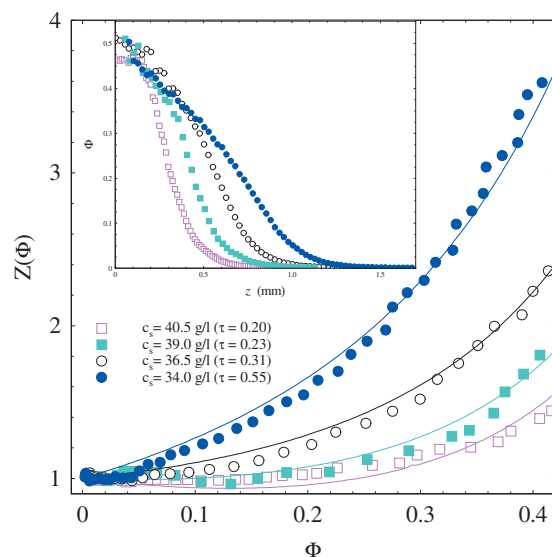

FIG. 5. Main body: compressibility factor $Z(\Phi)$ of the colloidal suspension at constant (20 mM) salt concentration and several values of c_s, corresponding to the four state points along the vertical line in Fig. 4. Each curve is fitted by the EOS of the Baxter model, and the best fit values of the stickiness parameter τ are given in the legend. The corresponding sedimentation profiles are shown in the inset.

C. Phase coexistence

Within our basic picture, the measurements reported in Fig. 4 yield the micellar concentration needed to cross the metastable spinodal line at low particle concentration, but they do not give any detailed information on colloidal phase coexistence. With the aim of mapping the full L-L coexistence curve, we have then tried and determined the composition of the coexisting phases obtained by separating samples prepared at an initial MFA particle volume fraction of $\Phi = 0.25$, which is quite close to the value numerically obtained for the critical density of the Baxter model.[21] Specifically, we shall compare results obtained for two series of samples, respectively, without salt and in the presence of 100 mM NaCl and a variable amount of added SDS.

A very concentrated mother batch (particle volume fraction of $\Phi_0 = 0.30 \pm 0.01$) was obtained by letting a moderately concentrated MFA suspension settle for a few months and retaining then only the dense sediment. This concentrated sample was brought to the prescribed state point by slowly adding a concentrated SDS/salt solution, stirring for 10–20 min to ensure full homogenization. Samples displaying phase separation show then a rapid turbidity increase, followed, on a time scale of a few minutes, by the formation of a clear meniscus. Similar to what was observed for irreversible colloidal aggregation,[29] the sample phase-separation kinetics can be roughly splitted into an initial stage of a few hours, when the meniscus descends at approximately constant velocity, followed by a much slower and approximately exponential sediment compression. The visual appearance of the salt-free sample series, 8 h after the beginning of phase separation, is shown at the top panel of Fig. 6. The main difference with respect to the sample shown in Fig. 1 is that the upper phases, at least for $c_s \gtrsim 26.5$ g/l, display evident scattering, witnessing that they are far from being totally
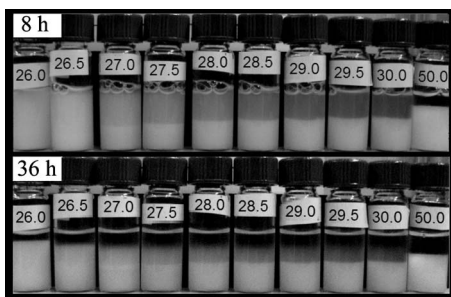
FIG. 6. Visual appearance of phase separated samples in the absence of added salt 8 and 36 h after sample preparation. The late stage of the process shows that, while the upper phase sediments as a fluid phase, the lower phases compress uniformly as colloidal gels.

depleted from particles. At this stage, we gently extracted a small amount from the upper phases and measured their density. This allows, knowing the sample volume partition and using the lever rule, one to obtain the volume fractions of both phases, which are shown at the top panel of Fig. 7.

As predicted for very short-ranged potential, the coexistence curve is very flat both in the absence of added salt and in the presence of 100 mM NaCl. Indeed, in both cases, the (quasicritical) surfactant concentration c_s^{cr} needed to induce phase separation at $\Phi = 0.25$, which we set as the mean between the values for the most concentrated stable suspension and the least concentrated separating sample, is only 10% lower than the value obtained at $\Phi = 0.02$. The substantial increase in depletion effects is, however, further witnessed by the reduction of about a factor of 2 in the absolute values of SDS concentration in the salt-free case.

The effective interaction between colloids can be conveniently represented as a square well potential of range δ (in units of the colloid diameter σ) and depth ϵ. We assume that
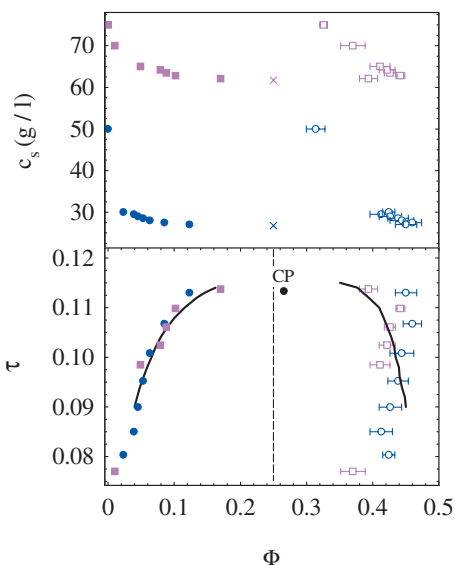

FIG. 7. Upper panel: concentration of the lower (open symbols) and upper (full symbols) phases at the end of the linear descent phase (8 h after sample mixing), in the absence of added salt (dots) and in the presence of 100 mM NaCl (squares). The crosses show the critical surfactant concentrations c_s^{cr} =26.8 and c_s^{cr}=61.7 g/l, respectively, found for the two sample series. The lower panel, where the full line is the Baxter spinodal curve numerically calculated in Ref. 21, shows the same data rescaled according to Eq. (5).

the range δ is on the order of the ratio between the micelle and the colloid radius, while the amplitude ϵ scales linearly with the depletant concentration c_s, as in the AO model. According to this picture, the full coexistence curve at different salt concentrations should collapse onto a single curve provided that the surfactant concentration is scaled with its critical value c_s^{cr}. In order to compare the experimental coexistence curves with the predictions of the AHS model,[21] it is useful to exploit the Noro–Frenkel extended principle of the corresponding states.[20] By defining a normalized temperature $T^* = k_B T / \epsilon$, the previously discussed relation between well depth and surfactant concentration can be formally written as

$$T^* = T_{cr}^* \frac{c_s^{cr}}{c_s} \tag{3}$$

in terms of the critical temperature T_{cr}^*, which, according to Ref. 20, scales as

$$T_{cr}^* \approx 0.26 + 2.1\delta \tag{4}$$

for δ not exceeding small. Finally, the stickiness parameter τ, which sets the strength of interparticle attraction in the Baxter model, is related to the range δ of a square well potential and to the normalized temperature T^* by

$$\tau = \frac{1}{4[(1+\delta)^3 - 1][\exp(1/T^*) - 1]}. \tag{5}$$

Equations (3)–(5) provide a correspondence between each c_s and τ. Figure 7 shows that, using $\delta = 0.04$, the dilute branch of both series nicely collapse onto the numerical results obtained in Ref. 21, confirming that, at least for $c_s \simeq c_s^{cr}$, our system can be quantitatively mapped onto the Baxter model.

The concentration of the dense phase, however, does not fall on the other branch of the coexistence curve for the Baxter model, and actually, for sufficiently low values of τ, seems to fall within the coexistence region. It is reasonable to assume therefore that they do not correspond to equilibrium phases but rather to arrested gel states. To our view, however, at variance with what has been claimed in Ref. 30, no physical relation between our data point and a metastable glass line penetrating into the coexistence region can be consistently attached. Had the experiments been made in density-matching conditions, as in Ref. 5, we would expect this gel phase, whose concentration is much larger than the percolation threshold, to span the whole sample volume as an arrested network coexisting with the dilute fluid phase.[31] Conversely, in the presence of gravity, the formation of a spanning network is hindered by the rapid sedimentation of large particle clusters, which settle and rearrange until they yield a suspension with a finite yield modulus. The arrested phase observed at the end of the linear settling period can therefore only be regarded as the least concentrated, approximately uniform gel phase possessing a sufficiently modulus to sustain gravity. Its concentration depends, however, on the density mismatch between particles and solvent. The following slow rearrangement period, lasting much longer, corresponds to plastic compression of the gel, yielding nonuniform concentration profiles such as those studied in Ref. 4.

V. THEORETICAL ANALYSIS

We now attempt an interpretation of the experimental results in the framework of classical statistical mechanics and liquid state theory, starting from a microscopic description of the colloidal suspension. The system is modeled as a binary mixture of charged particles—colloids and micelles—dispersed in an electrolyte. The mixture is then mapped onto a one-component fluid model by defining an effective colloid-colloid interaction mediated by the micelles. This step is accomplished by using the hypernetted-chain (HNC) equation from the theory of simple liquids. Finally, the EOS and phase portrait of the effective one-component fluid are determined and compared with the available experimental data.

A. Electrostatic interactions and model system

We consider a homogeneous dispersion of colloids and micelles in an electrolyte at room temperature. Here and in the following, the subscripts b and s will denote quantities related to the colloids (the *big* species) and the micelles (the *small* species), respectively, whereas the Greek indices μ and ν will be used to refer either species.

Both the colloids and the micelles are represented as charged hard spherical particles with diameter σ_μ, radius $a_\mu = \sigma_\mu/2$, and number density n_μ carrying a net negative charge $-Z_\mu e$, with e being the elementary charge. Considering the colloids as charged hard spheres is a standard procedure, while, within the DLVO picture, the intermicellar interaction should also include dispersion forces. However, Coulomb repulsion between micelles dominates in most of the experimentally investigated range; according to previous studies,[16] induced dipole-dipole forces become relevant at relatively high ionic strengths ($I \gtrsim 0.2$ monovalent salt moles/l). Therefore, to minimize the number of parameters in the model, micelles are considered as charged spheres, neglecting dispersion forces.

Electrostatic interactions in colloidal dispersions are deeply affected by screening from mobile charges in the solution, which include (i) positive and negative ions resulting from the dissolution of a salt of bulk molar concentration c_{salt}; (ii) the cmc contribution due to free SDS surfactant molecules; and (iii) positive counterions released by the colloids and the micelles. In the following, we shall neglect the colloid counterions because their contribution is always negligible at the concentration values we investigated. The relevant parameter governing the amount of mobile charges is the ionic strength I, which, under the hypothesis of monovalent ions, is given by (in moles per unit volume)

$$I = c_{salt} + cmc + \frac{Z_s^{eff} n_s}{2 N_A}, \tag{6}$$

where N_A is the Avogadro number and Z_s^{eff} is the number of *mobile* counterions released by each micelle.

The structure of the counterion cloud around a charged particle and the resulting screened Coulomb interaction between two charged spheres in solution is a classical problem of statistical physics[32] which has been studied by several approaches over the years, ranging from numerical simula-

tions, to Poisson–Boltzmann equation or phenomenological approaches. A key quantity characterizing the screening cloud at a surface is the inverse Debye length κ, defined as

$$\kappa = \sqrt{8 \pi l_B N_A I}, \tag{7}$$

where l_B is the Bjerrum length

$$l_B = \frac{\beta e^2}{\epsilon}, \tag{8}$$

β is the inverse thermal energy, and ϵ is the relative permittivity of the solvent.[33] The extent of screening of a charged sphere of radius a embedded in an electrolyte is then expressed by the dimensionless ratio κa between the sphere radius and the Debye length. In the parameter range of the experiments, this dimensionless quantity is always comparable to or larger than unity for both micelles and colloids, showing that the Debye length is the smallest length scale in our problem.

The electrostatic potential $\psi(r)$ of a single charged particle embedded in an electrolyte is usually expressed in a dimensionless form $\phi(r)$ by using the thermal potential $1/\beta e$. The geometry of the screening cloud is governed by the Poisson–Boltzmann equation with boundary condition at the sphere surface defined by the structural charge $Z^{str} = -a^2 \phi'(a)/l_B$. For $Z^{str} \gg 1$ and $\kappa a \gtrsim 1$, the screening cloud is dominated by nonlinear effects close to the surface of the sphere: *ion condensation* takes place in this region and the running charge quickly drops from the bare value (Z^{str}) to a much smaller limit (Z^{eff}), which depends only on the sphere radius,[32]

$$Z^{eff} \sim 4 \frac{a}{l_B}. \tag{9}$$

This effective charge therefore represents an estimate of the amount of *mobile ions* in the screening cloud around the sphere of radius a. Beyond this nonlinear region, the solution of the Poisson–Boltzmann equation is well represented by a simple Yukawa form

$$\beta \phi^{DH}(r) = y \frac{\exp[-\kappa(r-a)]}{r/a} \tag{10}$$

with an amplitude y weakly depending on the parameter $\kappa a \gtrsim 1$ and approaching $y = 4$ for sufficiently large structural charge: the amplitude y provides the effective surface potential which, in a Debye–Hückel approach, reproduces the asymptotic behavior of the solution to the full Poisson–Boltzmann equation. In Fig. 8 this distinctive behavior of the counterion cloud is illustrated for a representative choice of the parameter ($\kappa a = 2$ and $Z^{str} \rightarrow \infty$).

The previous discussion on the behavior of the screening cloud suggests that, for high structural charge and $\kappa a \gtrsim 1$, the electrostatic interactions between two spheres at the center to center distance r can be represented in a simple Debye–Hückel form
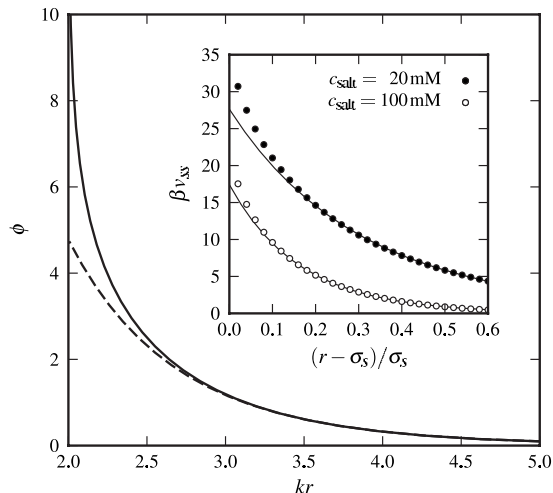
FIG. 8. (*Main body*) Numerical solution of the Poisson–Boltzmann equation in spherical symmetry for large structural charge $Z^{str} \to \infty$ and $\kappa a = 2$ (full line). The Yukawa form (10) representing the asymptotic decay at large distances is also shown (dashed line). (*Inset*) Comparison between the electrostatic interaction between two spheres obtained by numerical solution of the Poisson–Boltzmann equation (symbols) and the corresponding Yukawa potential (11) (full line).

$$\beta v^{DH}(r) = \frac{a}{2l_B} y^2 \frac{\exp[-\kappa(r-\sigma)]}{r/\sigma} \qquad (11)$$

provided that the surface to surface distance $r - \sigma$ is larger than the size of the condensed counterionic shell, where nonlinear effects prevail. We will therefore model the micelle through a purely repulsive interaction $v_{ss}(r)$ comprising of hard-sphere exclusion and Coulomb repulsion, represented in the Yukawa form (11).

To corroborate this choice, we directly evaluated the electrostatic interaction between two spheres with a uniform charge Z^{str} on their surface by numerical integration of the Poisson–Boltzmann equation in cylindrical symmetry. The results are shown in the inset of Fig. 8 for a choice of the parameters appropriate to model SDS micelles ($a_s = 2.5$ nm and $Z^{str} = 80$) in a solution of salt concentrations $c_{salt} = 20$ mM and $c_{salt} = 100$ mM. The effective interaction is well represented by a simple Yukawa form with amplitude y determined by a simple matching condition on the decay of the electrostatic potential $\phi(r)$ of a single sphere (10).

We tried and validate these theoretical expectations by performing static light scattering experiments on aqueous SDS solutions at low concentration and different ionic strengths. Following the seminal work by Corti and Degiorgio,[16] accurate light scattering data allow one to extract the dimensionless virial coefficient B_2^*, directly related to the screened intermicellar interaction by

$$B_2^* = 12\sigma_s^{-3} \int_0^\infty dr\, r^2 (1 - e^{-\beta v_{ss}(r)}). \qquad (12)$$

The experimental data are shown in Fig. 9, together with previous results available in literature.[16,34] To convert the directly accessible SDS weight fraction into a micelle number density and then to the micelle volume fraction $\Phi_s = (\pi/6)n_s\sigma_s^3$, it is necessary to estimate the micelle specific volume v. Neutron scattering data reported in Ref. 35 sug-
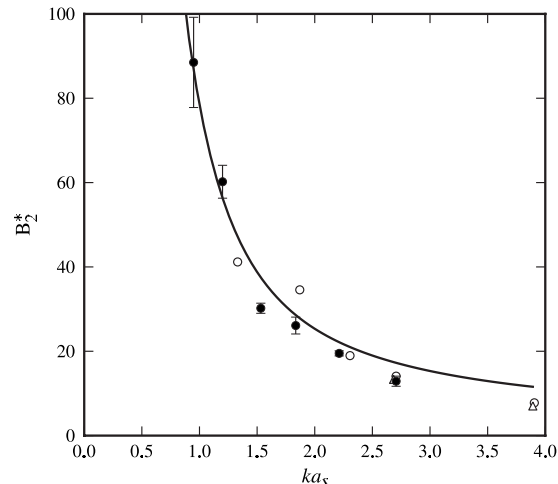

FIG. 9. Experimentally determined dimensionless virial coefficients of SDS in water solution at different salt concentrations as a function of κa_s. Full dots: this work; open dots from Ref. 34; open triangles form Ref. 16. Theoretical results (full line) obtained via Eq. (12) by modeling the system as a hard-sphere Yukawa fluid. The choice of parameters is discussed in the text.

gest that $v \sim 1.5 \pm 0.2$ cm^3/g, which we will consistently adopt in the comparison between theoretical results and experiments. The micelle properties entering our model potential (11) are just radius and effective surface potential y_s which we derive from known properties of SDS micelles in the following way: (i) the aggregation number as a function of the ionic strength is deduced from neutron scattering data;[35] (ii) the structural charge Z^{str} follows directly, attributing a single negative charge to each molecule; (iii) numerical integration of the Poisson–Boltzmann equation for each ionic strength provides the parameter y_s determining the amplitude of the Debye–Hückel potential (11); and (iv) the particle radius is assumed to grow with the ionic strength as the cubic root of the aggregation number: this keeps the specific volume v constant. The agreement between our simplified theoretical model and different sets of experimental data of Fig. 9 is rather good except at the highest ionic strengths, where dispersion forces are expected to play a relevant role, eventually leading to phase separation at $I \sim 400$ mM.

The electrostatic energy of the interaction of two colloidal particles, whose radii are much larger than the screening length, is usually modeled within Derjaguin approximation[36,37]

$$\beta v_{bb}(r) = \frac{a_b}{2l_B} y_b^2 \log[1 + e^{-\kappa(r-\sigma_b)}] \qquad (13)$$

in the physically accessible region $r > \sigma_b$. On the basis of the previously discussed arguments, we again expect that provided the colloidal charge is high enough, the parameter y_b will be close to its limiting value $y_b \sim 4$.

Finally, the colloid-micelle interaction, besides the exclusion due to the hard cores, is again determined by the geometry of the screening cloud. The resulting repulsive potential turns out to play an important role in the phase diagram of our model. On physical grounds, we expect a strong, almost hard-sphere, Coulomb repulsion at distances on the

order of the Debye length, followed by a softer repulsion at larger distances, well represented by a Yukawa form

$$\beta v_{bs}(h) = \frac{a_b a_s}{l_B} y_b y_s \frac{e^{-\kappa h}}{a_b + a_s + h}, \tag{14}$$

where $h = r - a_b - a_s$ is the distance between the surfaces of the two particles. An analytical expression embodying both the strong short-ranged repulsion at $h \lesssim 1/\kappa$ and the Yukawa tail is provided by the Hogg–Healy–Fuerstenau form,[38] giving the electrostatic energy of interaction of two particles with different radii at constant surface charge

$$\beta v_{bs}(h) = \frac{1}{4l_B} \frac{a_b a_s}{a_b + a_s + h} [4 y_b y_s \,\mathrm{atanh}(e^{-\kappa h})$$
$$+ - (y_b^2 + y_s^2) \log(1 - e^{-2\kappa h})]. \tag{15}$$

It should be clear that the model we are considering is not intended as a fully quantitative description of the physical system due to the crude representation of a colloid-micelle suspension as a mixture of charged hard spheres and to the adopted approximation in the description of the screening effects. Nevertheless, we expect that this theoretical framework is able to capture the essential nature of the interactions and to reproduce the key features seen in the experiments.

B. Generalities on effective interactions

When dealing with mixtures whose components are very asymmetric in size, it is customary to map the system onto an equivalent one-component fluid, which is often far easier to deal with, comprising particles of the larger species interacting via effective potentials accounting for the indirect contributions from the neglected components.

The reduction in a binary mixture to a one-component system is performed by a partial trace in phase space over the degrees of freedom of the particles belonging to the smaller species. More precisely, let H be the configurational energy of the mixture,

$$H(\mathbf{R}, \mathbf{r}) = H_{bb}(\mathbf{R}) + H_{ss}(\mathbf{r}) + H_{bs}(\mathbf{R}, \mathbf{r}), \tag{16}$$

where $\mathbf{R} = \{R_i\}_{i=1,\dots,N_b}$ and $\mathbf{r} = \{r_i\}_{i=1,\dots,N_s}$ are the set of coordinates of the big and the small particles, respectively, and the interactions are assumed as pairwise additive,

$$H_{bb}(\mathbf{R}) = \sum_{i<j}^{N_b} v_{bb}(|R_i - R_j|), \tag{17a}$$

$$H_{ss}(\mathbf{r}) = \sum_{i<j}^{N_s} v_{ss}(|r_i - r_j|), \tag{17b}$$

$$H_{bs}(\mathbf{R}, \mathbf{r}) = \sum_{i=1}^{N_b} \sum_{j=1}^{N_s} v_{bs}(|R_i - r_j|). \tag{17c}$$

In the semigrand ensemble, where the number N_b of the big particles and the fugacity z_s of the small particles are fixed, the free energy is expressed as

$$\exp[-\beta F(N_b, z_s, V)] = \mathrm{Tr}_{\mathbf{R}, \mathbf{r}} \exp[-\beta H], \tag{18}$$

where V is the volume of the system, the temperature dependence is implied, and the trace denotes the statistical average appropriate for the ensemble. By partitioning the trace over the degrees of freedom of the two species, the free energy can be written as

$$\exp[-\beta F] = \mathrm{Tr}_{\mathbf{R}} \exp[-\beta H^{\mathrm{eff}}], \tag{19}$$

where H^{eff} is an effective Hamiltonian depending on the coordinates of the big particles alone. It comprises the sum of two terms

$$H^{\mathrm{eff}} = H_{bb} + \Omega(N_b, z_s, V; \mathbf{R}), \tag{20}$$

the first accounting for the direct interactions, the second being the thermodynamic potential of a fluid of small particles in the external field imposed by a fixed configuration of the big ones,

$$\exp[-\beta \Omega] = \mathrm{Tr}_{\mathbf{r}} \exp[-\beta(H_{ss} + H_{bs})]. \tag{21}$$

It has been shown[39–41] that the potential Ω can be decomposed into a series of n-body terms $w^{(i)}$ so that the effective Hamiltonian takes the following form:

$$H^{\mathrm{eff}} = H^{(0)}(N_b, z_s, V) + \sum_{i<j}^{N_b} [v_{bb}(R_{ij}) + w^{(2)}(R_{ij}; z_2)]$$
$$+ \sum_{i<j<k}^{N_b} w^{(3)}(R_{ijk}; z_s) + \cdots, \tag{22}$$

where R_{ij} and R_{ijk} denote sets of two and three coordinates, respectively. $H^{(0)}$ is called the volume term and accounts for that part of the free energy of the small particles that does not depend on the position of the big ones. The pair term is the sum of the direct potential v_{bb} and the indirect contribution $w^{(2)}$ induced by the small spheres. Three-body and higher order terms are of indirect origin and entirely due to the species integrated out; in many cases, especially when the asymmetry between the two components is very large, they can be neglected to a good approximation.[42] The volume term is often neglected as well since it has a simple form linear in the volume and in the number of big particles resulting in innocuous shifts in the pressure and chemical potential that do not affect phase behavior.[41]

The one-component fluid with Hamiltonian H^{eff} and the original mixture share the same structure, as far as correlations between the big particles are concerned. For example, $S(k) = S_{bb}(k)$, where the first is the structure factor of the one-component system, whereas the second is the analogous quantity in the mixture. Thermodynamic properties are preserved as well so that any instability in the mixture shows up in the one-component picture too. These are the main points justifying the approach based on effective interactions.

C. Effective potential from HNC equations: Method and validation

Determination of the effective potential by direct computation of the partition sum in Eq. (21) is often not viable; a common alternative is to obtain the free energy of the small

particles at fixed configuration of the big ones, possibly with a certain degree of approximation, using other tools such as density functional theory or perturbation theory. Here we employ an approach based on integral equations from the theory of simple liquids, leading directly to the pair term of the effective potential.

It is known that in a homogeneous one-component fluid the zero density limit of the radial distribution function equals the Boltzmann factor of the two-body term in the interaction potential:[43] the same property holds in the mixture

$$\lim_{n_b \to 0} g_{bb}(r; n_b, z_s) = \exp\{-\beta[v_{bb}(r) + w^{(2)}(r; z_2)]\}$$
$$\doteq \exp[-\beta V^{\text{eff}}(r; z_s)], \tag{23}$$

where g_{bb} is the radial distribution function of the large particles and we defined V^{eff} as the two-body term of the effective potential. Thus, the latter is known once the correlations between the particles in the mixture are calculated at the pair level.

To obtain the correlations, we consider the Ornstein–Zernike relations for the mixture[43] in the limit of vanishing density of the large particles,

$$h_{ss}(r) = c_{ss}(r) + n_s^r[c_{ss} * h_{ss}](r), \tag{24a}$$

$$h_{bs}(r) = c_{bs}(r) + n_s^r[c_{bs} * h_{ss}](r), \tag{24b}$$

$$h_{bb}(r) = c_{bb}(r) + n_s^r[c_{bs} * h_{sb}](r). \tag{24c}$$

Here, $h_{\mu\nu} = g_{\mu\nu} - 1$ and $c_{\mu\nu}$ are the sets of total and direct correlation functions, the symbol $*$ denotes the three-dimensional product of convolution and n_s^r is the so-called reservoir density of the small particles, defined as the density of particles in a system comprising the small species alone in osmotic equilibrium with the mixture at a given composition.

Let us briefly discuss the role of the reservoir. In real experiments, it is natural to fix the composition of the mixture, specifying both densities n_b and n_s. This means that in the semigrand ensemble (18), the fugacity z_s of the small species has to be chosen so that the mean number density of particles equals the experimental value. From standard thermodynamics, the connection between the two quantities is

$$n_s(z_s, n_b) = -\frac{z_s}{V} \frac{\partial \beta F}{\partial z_s}. \tag{25}$$

The limiting procedure in Eq. (23) is carried out at fixed fugacity of the small particles; consequently, the density appearing in the Ornstein–Zernike relation (24) corresponds to the prescribed fugacity in the absence of large particles,

$$n_s^r(z_s) = \lim_{n_b \to 0} n_s(z_s, n_b). \tag{26}$$

This is the definition of the reservoir density. The exact relation between n_s and n_s^r is nontrivial, as manifested from Eq. (25); however, an asymptotic result can be derived
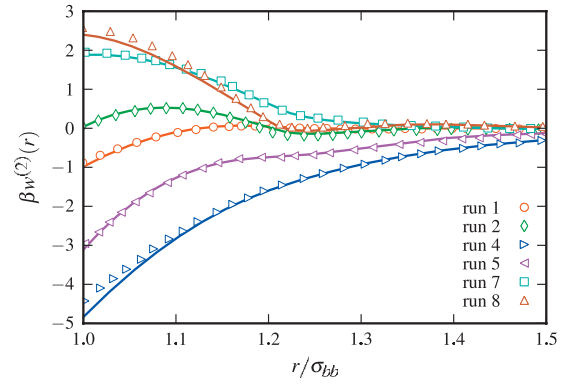

FIG. 10. Comparison of the effective potential as computed from the HNC equations and simulation data from Ref. 13. Big particles behave as hard spheres with diameter σ_{bb}, whereas b-s and s-s pair interactions have a hard-core Yukawa form with contact values $\epsilon_{\mu\nu}$, hard-core diameters $\sigma_{\mu\nu}$, and inverse decay lengths $\kappa_{\mu\nu}$. The strength of the Yukawa form is varied across the various runs (for details see the reference); the other parameters are fixed as follows: $\sigma_{ss} = \sigma_{bb}/5$, $\sigma_{bs} = (\sigma_{bb} + \sigma_{ss})/2$, $\kappa_{ss} = 15/\sigma_{bb}$, and $\kappa_{bs} = 6/\sigma_{bb}$; the packing fraction of the small particles is $\Phi_s = 0.1$. The symbols denote simulation data, whereas the lines are the results of HNC calculations.

$$\frac{n_s}{n_s^r} = 1 + n_b \int d\mathbf{r}\, h_{sb}(r) + O(\Phi_b^2), \tag{27}$$

where $h_{sb}(r)$ is the micelle-colloid radial correlation function appearing in the Ornstein–Zernike relation (24), the integration extends over all space and $\Phi_b = (\pi/6)n_b\sigma_b^3$ is the volume fraction of the large particles. In the following, we will drop the quadratic term and make use of the expression exact to linear order in Φ_b.

We supplement the Ornstein–Zernike equation (24) with the HNC closure[43]

$$\log g_{\mu\nu}(r) = -\beta v_{\mu\nu}(r) + h_{\mu\nu}(r) - c_{\mu\nu}(r). \tag{28}$$

The procedure to compute the pair term of the effective potential can be summarized as follows: (i) first, Eq. (24a) is solved, together with its closure, to obtain the correlation function h_{ss} of the small particles alone. (ii) The result is then inserted into Eq. (24b) to get the mixed correlation functions h_{bs} and c_{bs}. (iii) Finally, the sought-for-quantity $w^{(2)}$ follows from Eqs. (23), (24c), and (28),

$$-\beta w^{(2)}(r; z_2) = n_s^r(z_s)[c_{bs} * h_{sb}](r). \tag{29}$$

Equations (24a) and (24b) are solved numerically by means of a simple iterative scheme,[44] and convolutions are computed in Fourier space using a FFT algorithm.

To validate the method, we compare in Fig. 10 the pair term of the effective potential as obtained from simulations in Ref. 13 with the results of HNC calculations: the agreement is good, especially when both small-small and big-small interactions are repulsive (as in the case of interest).

D. Comparison with experimental data

We now turn to the evaluation of the effective colloid-colloid interaction which originates within the model discussed in Sec. V A. While in the simple AO model[6] of colloid-polymer mixtures the depletion mechanism leads unambiguously to an effective attraction between the colloids,

the effect of added big-small and small-small interactions on the depletion potential is a subject of extensive research and active debate in literature. On physical grounds, we expect that micelle-micelle repulsion leads to a larger pressure on the colloid surface, leading to stronger attraction via depletion mechanism. This effect is then predicted to enhance colloidal aggregation by lowering the ionic strength. However, the direct colloid repulsion contrasts this tendency and it is not clear which mechanism prevails in the experimental system. Furthermore, correlations induced by repulsive short-ranged interactions will also play a role in structuring the effective colloid-colloid interaction.

Depletion effects in interacting mixtures have been already considered in other systems: in Ref. 13, the authors found that the big-small repulsion results in a strongly enhanced effective attraction, whereas repulsion among the small particles triggers an accumulation near the surface of the big ones, preventing their aggregation. Experiments by Tohver and co-workers[45] show that charged nanoparticle halos surrounding colloidal particles can stabilize the dispersion against flocculation; the same phenomenon is seen in simulations[46] and in studies using integral equations techniques.[47] Let us point out a number of differences between the present case and the cited works: (i) in Refs. 13, 46, and 47 the big particles behave as pure hard spheres, whereas here an additional electrostatic repulsion is considered; (ii) the big-small interaction in the present model is repulsive, while in Ref. 46 is taken as attractive; (iii) in contrast to Refs. 13 and 47, the amplitudes of the bare interactions cannot be varied independently in our model since they exhibit a mutual dependence on the set of parameters.

Let us now discuss the different contributions to the effective colloid-colloid potential and their dependence on the model parameters. We first consider the simplest case of vanishing charge of the depletant, appropriate for describing charged MFA colloids in nonionic surfactant: the system experimentally studied in Sec. III. Due to the uncertainties in the modeling of the interactions between Triton micelles, we limit our investigation to the simplest case of ideal depletant by neglecting excluded volume and dispersion forces among the small particles. Thus, the effective interaction equals the sum of an attractive, salt-independent AO term and the repulsive screened potential (13); the amount of surfactant required to drive phase separation is expected to rise as the salt concentration is lowered, as clearly seen in the experiments. This behavior is indeed consistently reproduced in the simple AO/Coulomb system, as shown in Fig. 11.

Now we turn to the model relevant for MFA colloids in SDS ionic depletant. In Fig. 12 we show how the effective interaction is affected by the surface potential y_s of the small particles, for a fixed choice of the other parameters. When y_s is small, the interaction has a weak attractive well, while at small distances, the direct Coulomb repulsion between the colloids prevails.[48] As y_s is increased, several features appear: (i) the effective potential becomes more and more attractive, witnessing strong adhesion of the colloids; (ii) a repulsive barrier, whose height increases with the charge, develops in correspondence to higher values of the separation between the particles; (iii) secondary maxima and
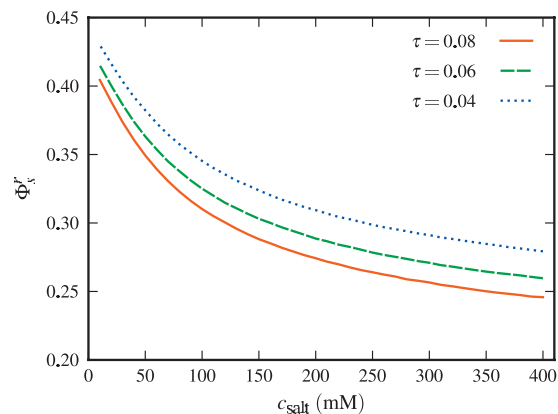

FIG. 11. Reservoir density of an ideal depletant required to induce an effective colloid-colloid interaction with a prescribed stickiness parameter τ [see Eq. (30)] as a function of salt concentration. The parameters are fixed as follows: $\sigma_b=180$ nm, $a_s=4.2$ nm, and $y_b=0.4$ in order to mimic the system studied in Sec. III, although we do not attempt a quantitative interpretation of experimental data.

minima appear for even larger distances. The deepening of the attractive well can be understood in a naive mechanical picture of the depletion mechanism: once two big particles are close enough, the pressure exerted by the sea of small particles, increasing with the charge, has to be overcome for them to be pulled apart. The growth of the barrier is due to an increase in correlations between the two species, as can be appreciated by looking at the mixed pair distribution function in the inset of the figure: if the charge of the small particles is raised, they accumulate more and more in the proximity of the big ones; since the overlapping of such charged clouds costs energy, the approach of two big particles is disfavored. This behavior has already been described in literature: it is termed "accumulation repulsion" in Ref. 13 and "nanoparticle haloing" in Refs. 45–47. Our results confirm the previous observations and provide an independent evidence for the phenomenon. In the present case, the accumulation takes place at a certain distance from the surface of the big particles and not right at contact: this is due to the unbound character of the potential (15), which prevents the touching of a big particle with a small one. We performed
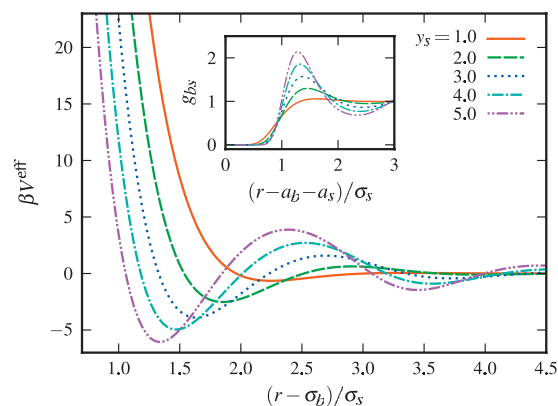

FIG. 12. Effective colloid-colloid interaction for different surface potential of the small particles, the other parameters being fixed at $a_s=2.5$ nm, $c_{salt}=20$ mM, $y_b=4$, and $\Phi_s^r=0.05$. Distances are expressed in units of the diameter of the small particles. In the inset, the big-small pair distribution function is shown.
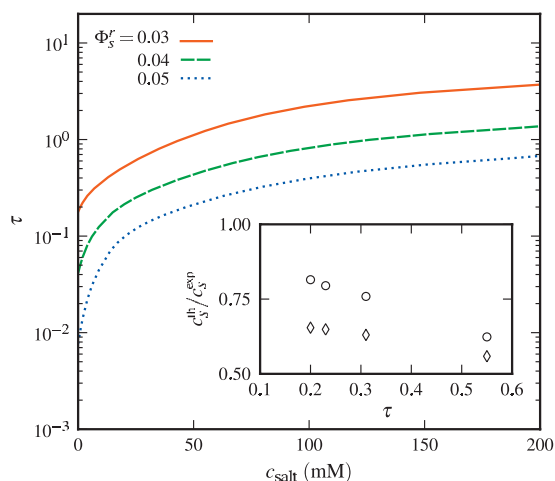
FIG. 13. Stickiness parameter τ of the effective colloidal one-component fluid as a function of the ionic strength of the solution at several volume fractions of the small particles. The inset shows the ratio between the theoretical estimate c_s^{th} and the experimental c_s^{exp} surfactant concentration corresponding to a given τ. Details in the text.

analogous calculations replacing the potential with a simple hard-core Yukawa having finite value at contact: in that case, accumulation happened right on the surface of the big particles and the repulsive barrier shifted toward contact as well, in agreement with Ref. 13.

Once the effective pair potential V^{eff} is known, the thermodynamic properties of the effective one-component fluid comprising the big particles alone can be obtained by several methods. When dealing with short-ranged interactions in colloidal systems, the Noro–Frenkel extended law of the corresponding states is usually invoked: the compressibility factor is a universal function of the reduced temperature, density, and of the reduced second virial coefficient B_2^*, but is independent of the specific shape of the potential.[20] Thus, the properties of the system of interest can be mapped onto those of an adhesive hard-sphere fluid with a stickiness parameter τ corresponding to the given B_2^*.[10] Values of τ close to zero signal a strong adhesion between the big particles, whereas large values point out a behavior akin to hard spheres. τ is defined in terms of the second virial coefficient of the colloids (12) by

$$\tau = \frac{1}{4 - B_2^*}. \tag{30}$$

The sticky sphere model has been extensively investigated in the past[21] and its phase diagram is by now well known, leading, via the Noro–Frenkel scaling, to a simple way to investigate the thermodynamic properties of this class of systems.

In Fig. 13 the dependence of the stickiness parameter of the effective potential on the ionic strength of the solution and on the density of the small particles is shown. To correctly evaluate the ionic strength, according to Eq. (6), we included the contribution due to the counterions released by the micelles by using Eq. (9) to estimate the number of counterion per micelle. Lowering the salt concentration, the bare electrostatic interactions become longer ranged and the effective potential becomes more attractive, leading to a smaller τ: this trend is consistently seen in the investigated

range of parameter space. The plot in Fig. 13 also shows that, at fixed ionic strength, raising the volume fraction of the small particles always causes the effective potential to become more attractive:[49] as before, this agrees with the experimental evidence.

By using the previously discussed value $v = 1.5$ cm^3/g for the specific volume of SDS micelles, we can directly compare these results with the experimentally determined EOSs of Fig. 5. The curves shown in Fig. 13 provide the "theoretical" micelle concentration c_s^{th} corresponding to a given value of the stickiness parameter τ. In the inset, we plot the ratio between the experimental concentration c_s^{expt}, also shown in Fig. 5, and this estimate, which follows from the analytical representation of the effective interaction between colloids mediated by the micelles (diamonds). Alternatively, following the discussion in Sec. IV C, we may evaluate the same ratio by using Eq. (5), which assumes a square well effective interaction. Fixing the potential width as $\delta = 0.04$, the value suggested by the collapse of the coexistence curves in Fig. 7, Eqs. (4) and (3) define a unique correspondence between each τ and a c_s. Ratios to the experimental values obtained according to this approach are shown by circles. The inset in Fig. 13 shows that both theoretical estimates of the surfactant concentration corresponding to a given τ underestimate the experimental results. The discrepancy may be partly attributed to the approximate representation of the experimental EOSs by the Baxter form. As already pointed out, the data shown in Fig. 5 suggest indeed that the EOS cannot be accurately represented in terms of an adhesive sphere model. However, to obtain a fully satisfactory agreement, we should also improve our modeling of electrostatic effects, particularly when strong asymmetries both in size and charge are present in the system.

If the experimentally observed aggregation of the colloidal particles is interpreted as a thermodynamic instability driven by the divergence of the isothermal compressibility, then the experimental transition points in the ($c_{rm\ salt}, c_s$) plane shown in Fig. 4 should correspond to the spinodal boundary at a fixed colloid volume fraction $\Phi_b = 0.02$. In the adhesive sphere model, this point of the spinodal line has not been directly investigated by numerical methods, while analytical approximations, such as the Percus–Yevick solution, are not reliable for these quantities. From the Monte Carlo simulations in Ref. 21, we can approximately locate the transition point at a stickiness parameter τ_t in the range of 0.04– 0.08. The dependence of τ on the physically accessible quantities ($c_{rm\ salt}, c_s$) has been evaluated from our effective colloid potential via Eq. (30) at different ionic strengths and surfactant concentrations. The results of the predicted transition line, evaluated for $\tau = 0.02$ and $\tau = 0.04$, are shown in Fig. 14 together with the experimental data in Fig. 4.

While the behavior at low ionic strengths is well reproduced, the theoretical curve seems to saturate before the experimental data at high salt concentration and, consistent with the previous analysis of the EOS, our model overestimates the attraction between colloids. Due to the uncertainties in the parameters and the gross simplifications of the adopted model, only a semiquantitative agreement can be obtained. However, the experimentally observed trend is
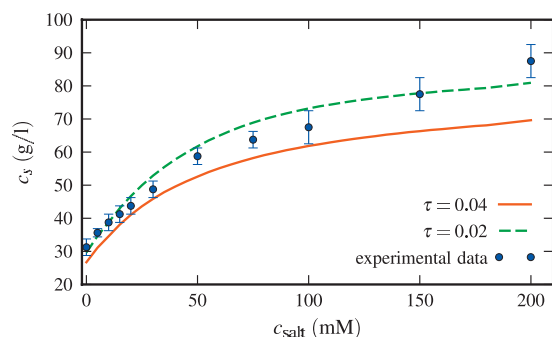
FIG. 14. Comparison between the experimental transition line and the loci of diverging compressibility from the mapping onto the Baxter model. The SDS volume fraction beyond which the colloids aggregate are shown as a function of the ionic strength of the solution. The two curves correspond to different values of the critical τ in the Baxter model.

clearly present also in our model, which, in fact, displays an enhanced tendency toward colloid aggregation when the electrostatic repulsion is poorly screened (at low ionic strength). This behavior is indeed robust and does not depend on the fine tuning of the model parameters.

VI. CONCLUSIONS

The experiments and their theoretical interpretation presented in this work display new and unexpected features in the phase diagrams of colloidal suspensions in the presence of interacting depletant. In charged surfactants, the repulsive potential can be modified by the addition of salt whose role is to screen the structural charge of the surfactant. This tunable interaction gives rise to a larger pressure in the micellar solution, enhancing the depletion effects. At the same time, it favors the accumulation of micelles near the colloids, leading to increasing correlations and then to more structured effective colloid-colloid interactions. As a consequence in charged colloidal solutions, a small amount of surfactant is able to trigger instability among colloids, leading to particle phase separation. The experimental EOSs obtained from sedimentation measurements are in moderate agreement with those predicted by the simple AHS model, and the dilute branch of the metastable L-L coexistence nicely satisfies the Noro–Frenkel criterion of the generalized corresponding states.

An accurate modeling of a colloidal suspension should include many physicochemical details which affect both micelle-micelle and micelle-colloid interactions. However, an extremely simple model including only electrostatic effects allows one to reproduce the experimentally observed trends. A consistent semiquantitative interpretation of the virial coefficients, the EOSs, and of the transition points as a function on the ionic strength can be achieved, with no fitting parameters, by requiring a large structural charge on colloids. The competition between screened Coulomb repulsion and depletion attraction leads to smooth effective colloid-colloid interactions depending quite sensitively on variations in the electrolyte properties. By tuning the ionic strength, it is then possible to enhance or inhibit colloidal aggregation, leading to a direct way to tailor phase diagrams of colloidal suspensions.

[1] W. C. K. Poon, Science **304**, 830 (2004).
[2] M. Dijkstra, J. M. Brader, and R. Evans, J. Phys.: Condens. Matter **11**, 10079 (1999).
[3] P. Charbonneau and D. R. Reichman, Phys. Rev. E **75**, 011507 (2007).
[4] S. Buzzaccaro, R. Rusconi, and R. Piazza, Phys. Rev. Lett. **99**, 098301 (2007).
[5] P. J. Lu, E. Zaccarelli, F. Ciulla, A. B. Schofield, F. Sciortino, and D. A. Weitz, Nature (London) **453**, 499 (2008).
[6] S. Asakura and F. Oosawa, J. Chem. Phys. **22**, 1255 (1954).
[7] R. Tuinier, J. Rieger, and C. G. de Kruif, Adv. Colloid Interface Sci. **103**, 1 (2003).
[8] H. N. W. Lekkerkerker, W. C. K. Poon, P. N. Pusey, A. Stroobants, and P. B. Warren, Europhys. Lett. **20**, 559 (1992).
[9] R. Verma, J. C. Crocker, T. C. Lubensky, and A. G. Yodh, Macromolecules **33**, 177 (2000).
[10] R. Baxter, J. Chem. Phys. **49**, 2770 (1968).
[11] R. Piazza, V. Peyre, and V. Degiorgio, Phys. Rev. E **58**, R2733 (1998).
[12] J. Bibette, D. Roux, and B. Pouligny, J. Phys. II **2**, 401 (1992).
[13] A. A. Louis, E. Allahyarov, H. Lowen, and R. Roth, Phys. Rev. E **65**, 061407 (2002).
[14] R. Roth, R. Evans, and L. L. Louis, Phys. Rev. E **64**, 051202 (2001).
[15] V. Degiorgio, R. Piazza, T. Bellini, and M. Visca, Adv. Colloid Interface Sci. **48**, 61 (1994).
[16] M. Corti and V. Degiorgio, J. Phys. Chem. **85**, 711 (1981).
[17] P. S. Goyal, S. V. G. Menon, B. A. Dasannacharya, and P. Thiyagarajan, Phys. Rev. E **51**, 2308 (1995).
[18] S. Buzzaccaro, A. Tripodi, R. Rusconi, D. Vigolo, and R. Piazza, J. Phys. Condens. Matter **20**, 494219 (2008).
[19] Note that, due to hydration, the volume fraction of *micelles* Φ_s is about 40% larger than the volume fraction of *surfactant* used in Ref. 4.
[20] M. G. Noro and D. Frenkel, J. Chem. Phys. **113**, 2941 (2000).
[21] M. A. Miller and D. Frenkel, J. Chem. Phys. **121**, 535 (2004).
[22] Here and in what follows, both the salt molarity and the surfactant concentration are referred to the *solvent* volume, i.e., without taking into account the volume occupied by the colloidal particles.
[23] M. Dijkstra, Phys. Rev. E **66**, 021402 (2002).
[24] F. Sciortino, S. Mossa, E. Zaccarelli, and P. Tartaglia, Phys. Rev. Lett. **93**, 055701 (2004).
[25] A. Imperio and L. Reatto, J. Chem. Phys. **124**, 164712 (2006).
[26] R. Sanchez and P. Bartlett, J. Phys. Condens. Matter **17**, S3551 (2005).
[27] A. Fortini, E. Sanz, and M. Dijkstra, Phys. Rev. E **78**, 041402 (2008).
[28] R. Piazza, M. Eghan, V. Peyre, and V. Degiorgio, Prog. Colloid Polym. Sci. **110**, 89 (1998).
[29] J.-M. Condre, C. Ligoure, and L. Cipelletti, J. Stat. Mech. **2007**, P02010.
[30] T. Gibaud and P. Schurtenberger, J. Phys. Condens. Matter **21**, 322201 (2009).
[31] Lu *et al.* (Ref. 5) showed that, in these conditions, a reasonable definition of the dense phase composition can be obtained by direct visualization of the cluster network.
[32] L. Belloni, Colloids Surf., A **140**, 227 (1998).
[33] The dielectric permittivity is the only parameter that contains the properties of the solvent, considered as an incompressible continuum medium.
[34] C. Thévenot, B. Grassl, G. Bastiat, and W. Binana, Colloids Surf., A **252**, 105 (2005).
[35] S. Bucci, C. Fagotti, V. Degiorgio, and R. Piazza, Langmuir **7**, 824 (1991).
[36] R. J. Hunter, *Foundation of Colloid Science*, 2nd ed. (Oxford University Press, Oxford, 1991).
[37] H. Ohshima, *Theory of Colloid and Interfacial Electric Phenomena* (Elsevier, Amsterdam, 2006).
[38] R. Hogg, T. W. Healy, and D. W. Fuerstenau, Trans. Faraday Soc. **62**, 1638 (1966).
[39] M. Dijkstra, R. van Roij, and R. Evans, Phys. Rev. E **59**, 5744 (1999).

[40] M. Dijkstra, R. van Roij, and R. Evans, Phys. Rev. Lett. **81**, 2268 (1998).

[41] M. Dijkstra, R. van Roij, and R. Evans, J. Chem. Phys. **113**, 4799 (2000).

[42] A. A. Louis, Philos. Trans. R. Soc. London, Ser. B **359**, 939 (2001).

[43] J. Hansen and I. R. McDonald, *Theory of Simple Liquids*, 2nd ed. (Elsevier, Amsterdam, 1986).

[44] K.-C. Ng, J. Chem. Phys. **61**, 2680 (1974).

[45] V. Tohver, A. Chan, O. Sakurada, and J. A. Lewis, Langmuir **17**, 8414 (2001).

[46] J. Liu and E. Luijten, Phys. Rev. Lett. **93**, 247802 (2004).

[47] S. Karanikas and A. Louis, Phys. Rev. Lett. **93**, 248303 (2004).

[48] Even if the particles have a hard core, we do not see the oscillatory behavior typical of hard-sphere mixtures since the packing fraction of the depletant is low.

[49] Unless a high-concentration regime is entered, not depicted in the figure nor sampled in the experiments, where the trend reverses due to correlation and packing effects of the small particles.